Optics Communications 383 (2017) 423–429

Contents lists available at ScienceDirect

Optics Communications

journal homepage: www.elsevier.com/locate/optcom

Converting surface plasmon polaritons into spatial bending beams through graded dielectric rectangles over metal film

Hui Li [a,b], Yongzheng Xu [a], Gang Wang [a], Tong Fu [a], Li Wang [a], Zhongyue Zhang [a,*]

[a] School of Physics and Information Technology, Shaanxi Normal University, Xi'an 710062, China
[b] Division of public infrastructure, De-hong Vocational College, Mang-shi 678400, China

ARTICLE INFO

Article history:
Received 17 July 2016
Received in revised form
12 September 2016
Accepted 20 September 2016

Keywords:
Surface plasmon polaritons
Spatial bending beams
Phase modulation
Finite-element method

ABSTRACT

Spatial bending beams, which preserve their spatial shape while propagating along curved trajectories in free space, offer important application in the fields of fiber sensor, optical trapping, and micro-manipulation. In this work, two slits are designed on a metal film to excite surface plasmon polaritons (SPPs), and a group of dielectric rectangles over metal film is theoretically proposed to directly convert SPPs into spatial beams showing arbitrary bending. The appropriate locations of the dielectric rectangles are calculated by phase-modulation method. Transverse acceleration and nondiffraction characteristics of spatial bending beams are observed. We further demonstrate that the intensity distribution, shape, and propagation length of spatial beams showing arbitrary bending rely on structural parameters of dielectric rectangles and on the distance between dielectric rectangles and metal film. These findings provide guidance in the design and optimization of bending beam generators.

1. Introduction

Spatial bending beams, which preserve their shapes while propagating along curved trajectories in free space, are attracting increased attention. These beams offer potential applications in the fields of optical trapping [1] and manipulation [2]. Airy wave packets [3–7], being typical bending beams, were studied in 2007 [3]. A new group of bending beams, including Bessel beam [8,9], Mathieu beam [10], Weber beam [11,12], Bessel-like beam [13], and other arbitrary bending beams [14,15], which are exact solutions of the non-paraxial Helmholtz equation [14,15], were subsequently introduced. These spatial bending beams can be classified into two groups, spatial bending beams in two-dimensional surface [13,15] and spatial bending beams in three-dimensional space [10–12].

Spatial bending beams in a two-dimensional system exist as surface plasmon polaritons (SPPs) wave [13,16]. SPPs are surface electromagnetic wave consisting of collective electron oscillations, which propagate along a metal-dielectric interface and decay in the direction of propagation [17,18]. Researchers recently realized SPPs-based spatial bending beams. For example, cosine-Gauss beam [19], which propagates in a straight line along metallic surface for distances of up to 80 μm, was demonstrated by a group of intersecting metal gratings. Airy beam, which propagates along a parabolic trajectory, was demonstrated by a nanoscale phase grating on a metal film [20–23]. Beams showing arbitrary bending were demonstrated through Bragg diffraction, which is designed using hole arrays on a silver surface [24–26]. Beams showing arbitrary bending (propagating along the trajectory of x^n, polynomial, and logarithmic) [27,28], Weber, and Mathieu beams (propagating along the trajectory of circle and ellipse) [29] are also generated by a two-dimensional binary phase mask [37].

Conversion of SPPs into beams in free space has been widely investigated. For example, various plasmonic lens [30–32,40] consisting of an array of nanoscale slits or an annular slit in metallic film were proposed to achieve far-field focusing. A free-space Airy beam was converted from SPPs by using the holographic method via Fourier transformation [33]. An Airy-like beam was converted from SPPs by using groove array and a single slit on a metal film-coated optical fiber facet [34–36]. These structures, being a group of compact converters, offer many advantages, such as flexibility and easy portability [35,36].

In this work, two slits are designed on a metal film to excite the SPPs propagating along metallic surface, and a group of dielectric rectangles are designed over a metal film to convert SPPs into spatial beams showing arbitrary bending. These dielectric rectangles, which form a group of nano-scatterers located at a proper location, are designed using the phase modulation method. Simulations revealed that the generated spatial beams showing arbitrary bending demonstrate nondiffraction and transverse acceleration. Furthermore, the effects of structural parameters on

* Corresponding author.
E-mail addresses: l.wang@snnu.edu.cn (L. Wang), zyzhang@snnu.edu.cn (Z. Zhang).

http://dx.doi.org/10.1016/j.optcom.2016.09.045
0030-4018/

spatial bending beams are investigated. All these findings can provide guidance in the design and optimization of bending beam generator.

2. Structure and calculation method

Fig. 1 shows the configuration of the dielectric rectangles on an Au/SiO_2 substrate. In this study, w is the width of dielectric rectangles, h is the height of the dielectric rectangles, d is the distance between rectangles and the interface of the gold film. The thickness and the width of the slits are fixed at 200 and 130 nm, respectively. The red block diagram illustrates a single dielectric rectangle above Au/SiO2 substrate and the relationship of structural parameters. In this work, the propagation properties of the spatial bending beams are simulated by a two-dimensional radio frequency module of the COMSOL Multiphysics software. COMSOL is a finite element analysis and solver software package for various physics and engineering applications. Scattering boundary condition is applied. Stationary direct solver is chosen. The sizes of elements are from 0.8 to 8 nm. In the meshing, there are no special treatments for corners. A plane wave at 0.98 μm wavelength with a magnitude of 1 v/m, polarization at x direction, is incident $(+y)$ into the slit. The relative permittivity ε_m of the gold film is $-36.4+3.26i$ at 0.98 μm [41]. Silicon is chosen as dielectric rectangles, and its refractive index is 3.476 [42].

SPPs excited in the slits propagate along the interface of the gold film and are decoupled into free space by dielectric rectangles. In this work, the dielectric rectangles, being a group of nano-scatterers located at an appropriate location, achieve a constructive scattering process to form the desired spatial beam showing arbitrary bending. The scattered wave E_S from each individual rectangle Λ_i can be written as a relation between the incident electric field E_0 and the total electric field E on the surface. E_S can be expressed as [37]

$$E_s(x, z) = E(x, z) - E_0(x, z) = A \iint k_0^2[\varepsilon_1(x', z') - \varepsilon_1(z')] \times G(x - x')E(x', z')d\Lambda_i, \quad (1)$$

where G is the Green's dyadic and ε_1 is the dielectric constants of the volume of rectangle Λ_i. Under the case of the far-field and considering a group of small rectangles Λ_i, the above expression (1) can be simplified as [37]

$$E_s \approx \iint k_0^2[\varepsilon_1(x', z') - \varepsilon_1(z')]\, E_1(x', z')d\Lambda_i \times \exp(-i\varphi_n(x)), \quad (2)$$

where $\varphi_n(x)$ is the phase contribution of the nth dielectric rectangles and can be deduced as

$$\varphi_n(x) = \varphi_0 + k_{spp}x - nw(k_{spp} - \beta) - 2n\pi, \quad (3)$$

where n is an integer, and φ_0 is the initial phase, and x is the distance of the nth dielectric rectangles from two slits, and 2π is an additional phase difference between neighboring dielectric rectangles. $k_{spp} = k_0\sqrt{\varepsilon_2\varepsilon_m/(\varepsilon_2 + \varepsilon_m)}$ is the wavevector of SPPs propagating on the film, k_0 is the free-space wavevector, and ε_2 and ε_m are the relative permittivity of the air and the gold film, respectively. β represents the wavevector of SPPs propagating between the rectangle and the film. Thus, βw represents an additional phase of SPPs propagating between the rectangle and the film. The space between rectangle and film can be considered as dielectric/air/metal $(\varepsilon_1/\varepsilon_2/\varepsilon_m)$ structure. The transverse magnetic mode of this structure follows the following dispersion relationship [38]:

$$\tanh(k_2\varepsilon_2 d) = -\frac{k_1k_2 + k_2k_m}{k_2^2 + k_1k_m}, \quad (4)$$

where d is the distance between dielectric rectangles and metal film, and $k_{1(2m)} = \sqrt{\beta^2 - \varepsilon_{1(2m)}k_0^2}/\varepsilon_{1(2m)}$. Hence, phase delay depends strongly on the distance between dielectric rectangles and metal film.

3. Results and discussion

Phase $\varphi(x)$ of the required spatial bending beam was calculated utilizing Legendre transform method [12,13,27–29,39]. The desired arbitrary bending trajectory (red line) is defined by $f(y)$ in Fig. 2(a), and phase $\varphi(x)$ is the spatial phase profile on the boundary (x axis). θ is the angle between y-axis and the tangent line through the point (x_0, y_0). A group of tangent lines emanating from point x_n generates a caustic. The geometric relationship between the phase and the angle θ can be deduced as

$$d\phi(x) = -k_0 \sin\theta dx, \quad (5)$$

where dx represents infinitesimal distance between two points along the x direction, $d\phi(x)$ and $dx\sin\theta$ represent the phase shift and optical path length difference respectively. In the case of non-paraxial, the trigonometric function $\sin\theta = \tan\theta/\sqrt{1 + \tan^2\theta}$ is exploited. In the case of paraxial approximation, $\sin\theta \approx \tan\theta$ is applied. The spatial phase can be obtained for paraxial and non-paraxial regimes [12,13],

$$\phi(x) = -\int k_0\tan\theta dx \quad (6)$$

and

$$\phi(x) = -\int k_0\tan\theta/\sqrt{1 + \tan^2\theta}\, dx, \quad (7)$$

where $-\tan\theta = f'(y)$, $f'(y)$ is the first-order derivative of f(y). The variable y can be eliminated with the intercept of the tangent line $x = x_0 + y_0\tan\theta$. The relationship between intercept x and the

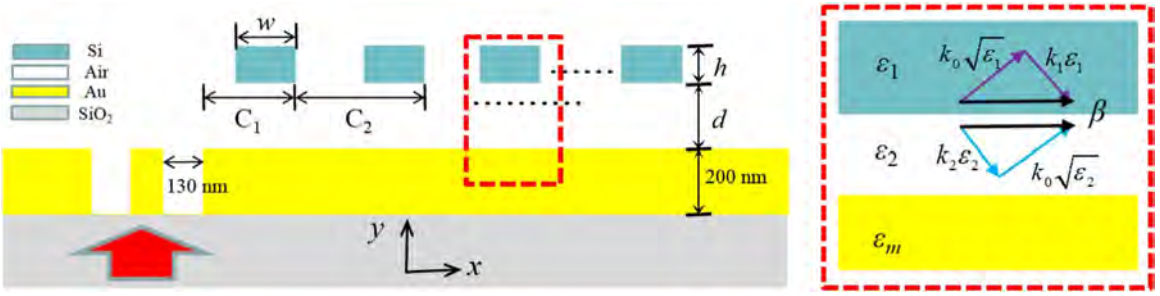

Fig. 1. The configuration of dielectric rectangles above Au/SiO_2 substrate. The red block diagram illustrates a single dielectric rectangle above Au/SiO_2 substrate and the relationship of structural parameters; where ε_1, ε_2 and ε_m represent the relative permittivity of Si, Air and the gold film respectively. The triangle rectangle represent the relationship of the components $k_{1(2)}\varepsilon_{1(2)}$, $k_0(\varepsilon_{1(2)})^{0.5}$ and β. (For interpretation of the references to color in this figure legend, the reader is referred to the web version of this article.)

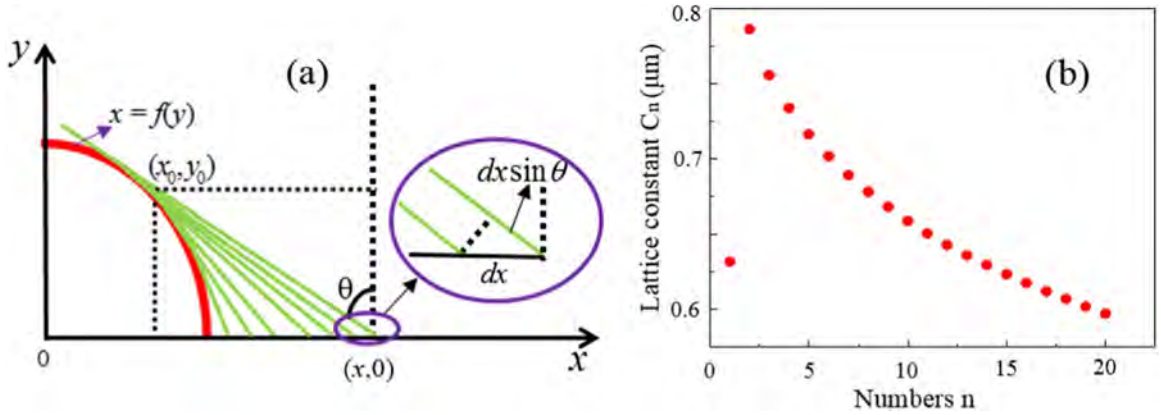

Fig. 2. (a) Illustration of an arbitrary bending trajectory $f(y)$ and the tangent line. (b) Calculated local lattice constant (C_n) of the dielectric rectangles. (For interpretation of the references to color in this figure, the reader is referred to the web version of this article.)

angle θ is also deduced as $\tan\theta = F(x)$. Detailed derivation of phase profile for paraxial and non-paraxial trajectory are shown in Supplementary material. For example, for the curve of $f(y) = -a_2y^2$, the required phase is $\phi(x) = -1.33k_0a_2x^{1.5}$, where k_0 is the wavevector of light in free space, the constant a_2 is equal to 5×10^{-3}. We can calculate every location of the dielectric rectangle by solving $\varphi_n(x) = \phi(x)$. The local lattice constant $C_n = x_n - x_{n-1}$ is calculated (Fig. 2(b)) when the number of dielectric rectangles is equal to 20.

Fig. 3(a) shows the intensity distribution of electric field in the x-y plane when the number of dielectric rectangles is equal to 20. The width and height of the dielectric rectangles are 260 and 80 nm, respectively. The distance between a rectangle and interface of the gold film is set as 60 nm. The inset illustrates steady-state electric-field distributions of single dielectric rectangle. Fig. 3(b) shows the transverse intensity distribution. The black solid curve depicts the parabolic curve $f(y)$. Fig. 3(c) shows distributions of surface current density in x-y plane. The main lobe intensity distribution is obviously consistent with the parabolic curve trajectory. These results show that the bending beam exhibits transverse acceleration and nondiffraction characteristics, and it can propagate at approximately 50 μm in free space. The electric field of the generated parabolic beam is mainly x-polarized. These results demonstrate that the desired spatial bending beams were converted through constructive scattering, wherein the dielectric rectangles are located above a metal film. To determine the effect of the distance d between a dielectric rectangle and metal film on spatial bending beams, the difference value for d at $h=80$ nm and $w=260$ nm is chosen. Intensity distribution under different d values is simulated in Fig. 4(a)–(c). The black solid curve depicts the target parabolic curve $f(y)$. As shown in Fig. 4(a), rectangles located close to the slits form the bottom part of the target curve, whereas those located far from the slits form the top part of the target curve. With the increase in d, more energy is transmitted to the rectangles located far from the slits, resulting in stronger intensity at the top part of the curve (Fig. 4(c)).

To determine the effect of w of dielectric rectangle on the spatial bending beams, the difference value for w at $h=80$ nm and $d=60$ nm is chosen. Intensity distribution is simulated in Fig. 5(a)–(c) under the following difference values for w: (a) $w=200$ nm, (b) $w=260$ nm, (c) $w=320$ nm. The black solid curve depicts the target parabolic curve $f(y)$. The bending beams are consistent with the target curves. As w increases, the intensity of the bending beams increases resulting from the increasing scattering of

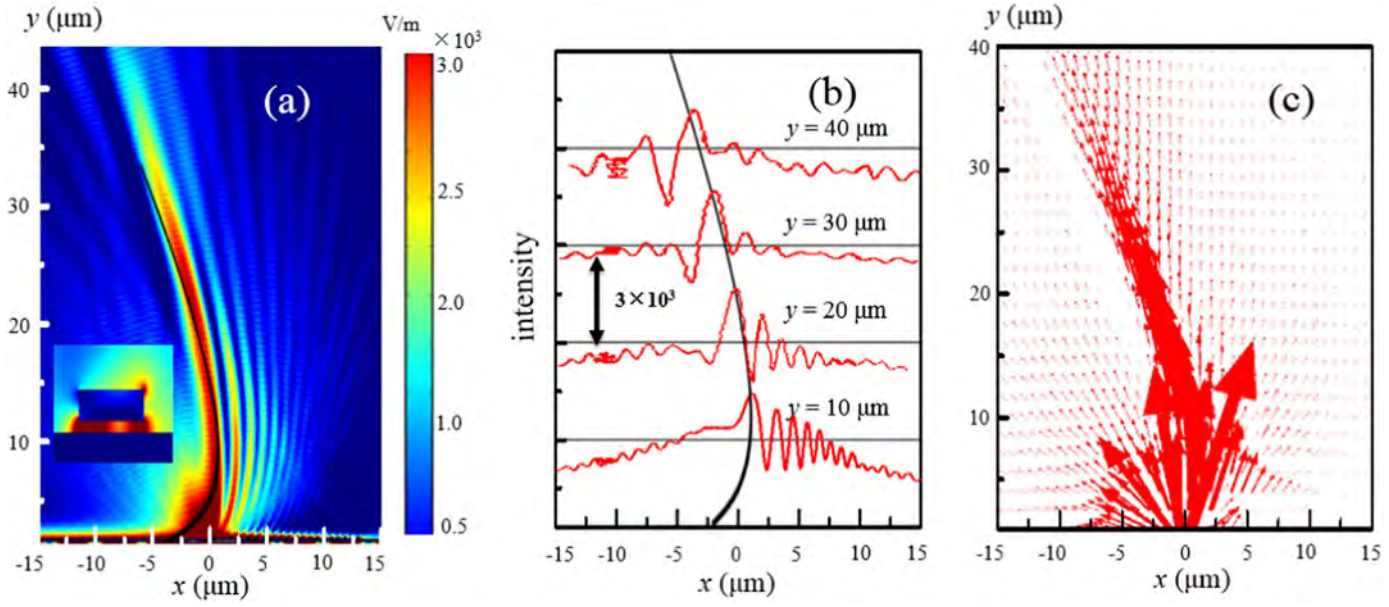

Fig. 3. (a) Simulation of the generated parabolic beam intensity distribution under the paraxial approximation; the inset illustrates steady-state electric-field distributions of single dielectric rectangle. (b) Transverse intensity distributions at different distances y, the black solid curve depict the bending curve $f(y) = -a_2y^2$, with $a_2 = 5\times10^{-3}$. (c) Distributions of surface current density in x-y plane.

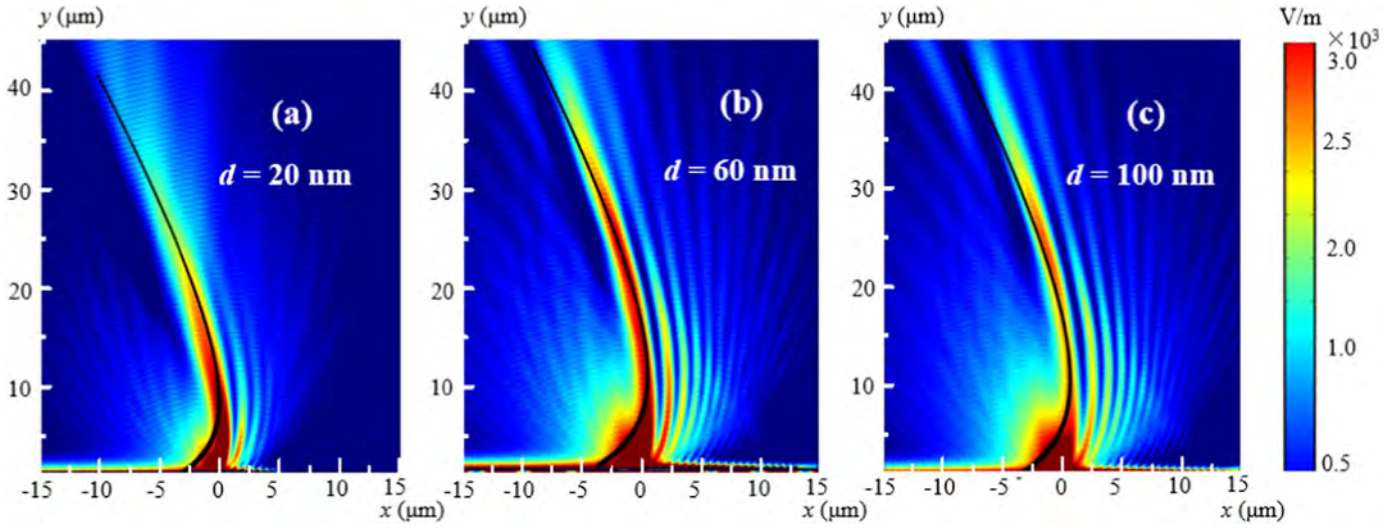

Fig. 4. (a)–(c) Simulation of the generated parabolic beam intensity distribution with $d=20$ nm, 60 nm and 100 nm.

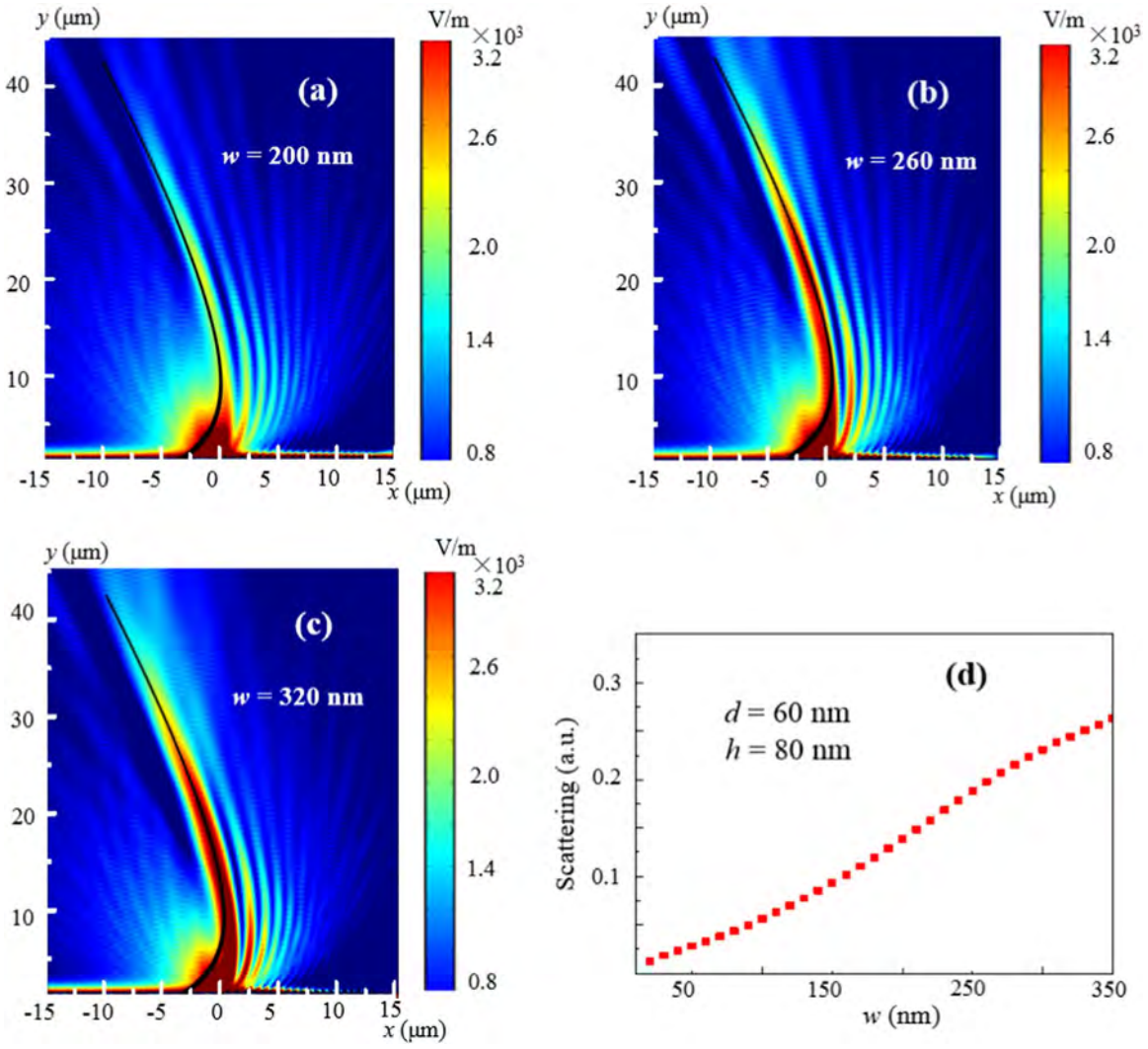

Fig. 5. (a)–(c) Simulation of the generated parabolic beam intensity distribution with difference width w=200 nm, 260 nm and 320 nm. (d) Calculated scattering of a single dielectric rectangle for different w with $d=60$ nm and $h=80$ nm.

rectangles (Fig. 5(d)).

To determine the effect of dielectric rectangle height h on conversion of SPPs into spatial bending beams, the difference value for h at $w=260$ nm and $d=60$ nm is chosen. Intensity distribution is simulated in Fig. 6(a)–(c) using the following difference values of h: (a) $h=60$ nm, (b) $h=80$ nm, and (c) $h=100$ nm. The

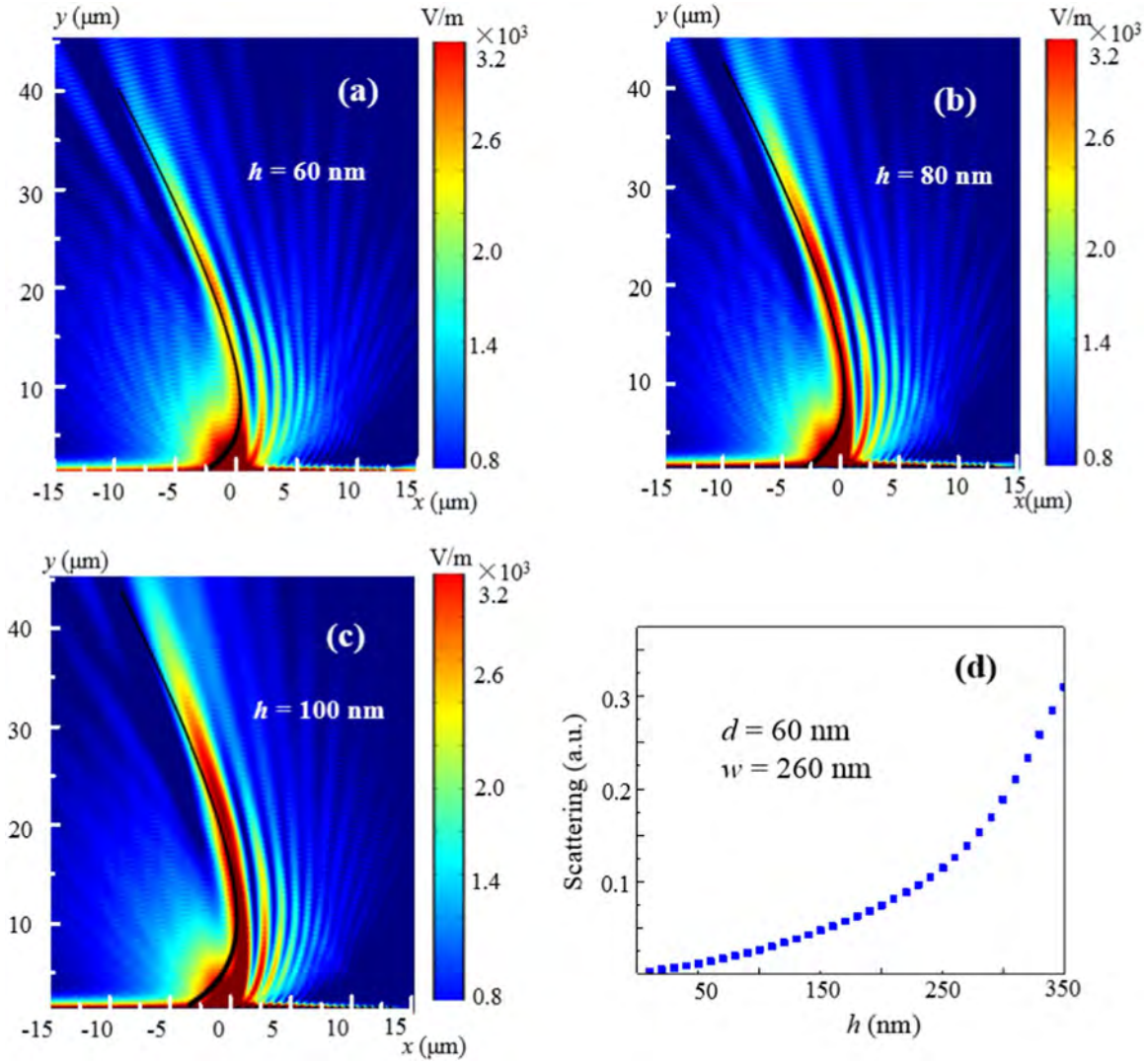

Fig. 6. (a)–(c) Simulation of the generated parabolic beam intensity distribution with difference width h=60 nm, 80 nm and 100 nm. (d) Calculated scattering of a single dielectric rectangle for different h with w=260 nm and d=60 nm.

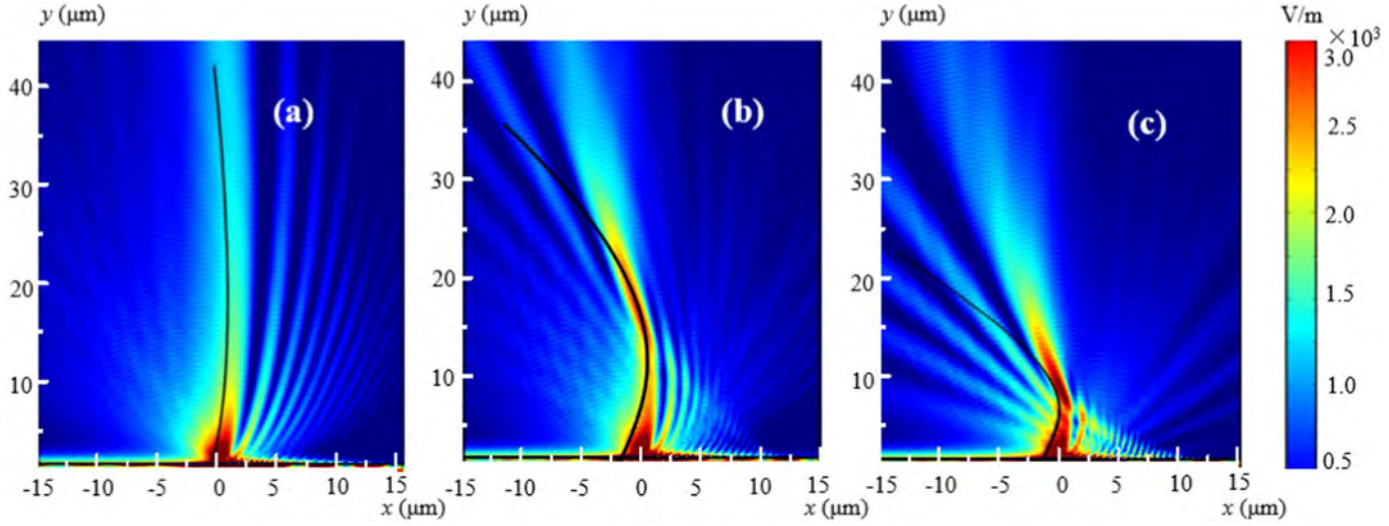

Fig. 7. Simulation of the generated bending beam intensity distribution under the paraxial approximation: (a) $f(y) = -a_{1.25}y^{1.25}$, with $a_{1.25} = 3 \times 10^{-2}$. (b) $f(y) = -a_3y^3$, with $a_3 = 3 \times 10^{-4}$. (c) $f(y) = -a_4y^4$, with $a_4 = 4 \times 10^{-4}$. The black solid curve depict the bending curves.

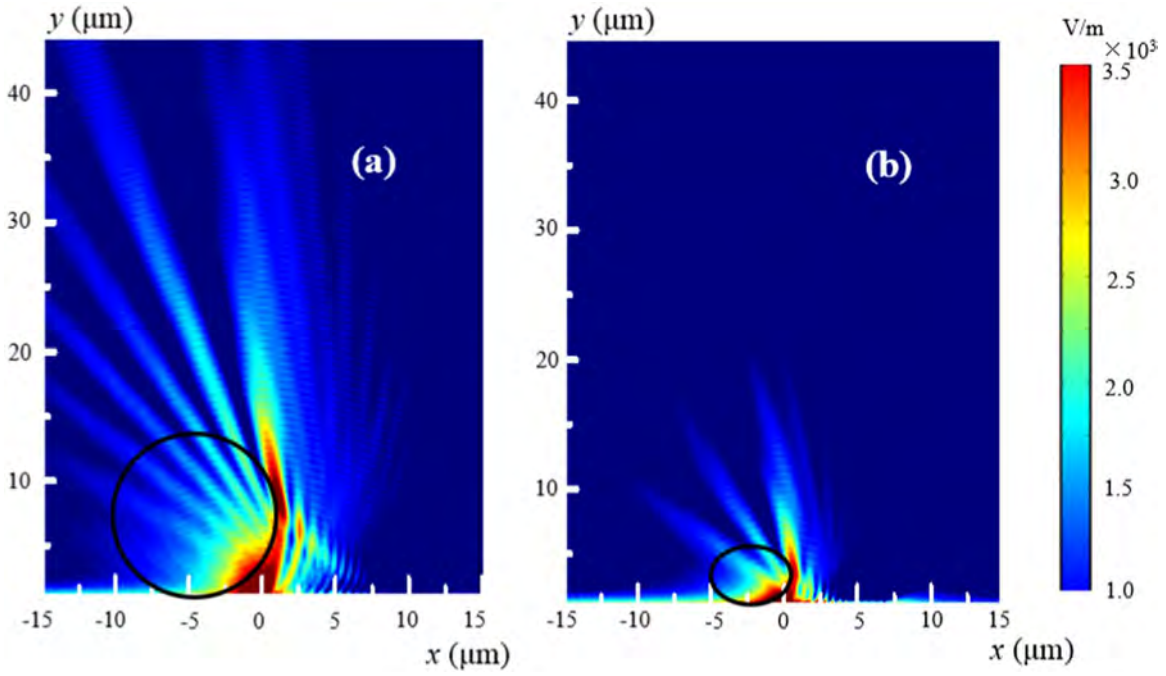

Fig. 8. Simulation of the generated beading beam intensity distribution under the paraxial approximation: (a) $f(y) = [r^2 - (y - r)^2]^{0.5}$, with the radius of circle $r=5$ μm. (b) $f(y) = m[1 - (y/q)^2]^{0.5}$, with the major of the ellipse $q=2$ μm, the minor axes of the ellipse $m=1$ μm. The black solid curve depict the circle curve and ellipse curve.

bending beams are consistent with the target curves. As h increases, the intensity of the bending beams increases resulting from the increasing scattering of rectangles (Fig. 6(d)).

Other spatial bending beams that follow the trajectory $f(y) = -a_n y^n$, with $n=1.25$, 3, 4, are also generated. The constant a_n is arbitrarily chosen following pre-designed trajectory intersection point [14]. For example, the bending beam follow the trajectory $f(y) = -a_3 y^3$intersect at $y=20$ μm, we obtain the constant $a_3 = 3 \times 10^{-4}$ by geometric relationship. Fig. 7 shows the simulated intensity distributions of the generated beading beam. The black solid curves depict the bending curve. The propagation of the different spatial bending beams obviously propagate along the designed curve trajectory.

The circular trajectory is defined as $f(y) = [r^2 - (y - r)^2]^{0.5}$ and the ellipse trajectory is defined as $f(y) = m[1 - (y/q)^2]^{0.5}$, where r is the radius of the circle, and m and q are the major and minor axes of the ellipse, respectively. Fig. 8 shows the simulation of the intensity distribution of the generated bending beam in the x-y plane. The black solid curve depicts the designed circle curve and ellipse curve. The bending beams obviously propagate along the designed circular trajectory (Fig. 8(a)), where $r=5$ μm, and along the ellipse trajectory (Fig. 8(b)), where $q=2$ μm and $m=1$ μm, demonstrating our capability to form light beams that accelerate along any convex curve $f(y)$.

4. Conclusions

The spatial beams showing arbitrary bending were converted by graded dielectric rectangles located on a metal film. By introducing dielectric rectangles as a group of nano-scatterers at the proper location by using the phase modulation method, we achieved a constructive scattering process to form desired spatial beams with arbitrary bending. The result shows that the shape of the spatial bending beam is consistent with that of the target bending curve. The effects of structural parameters on spatial beams with arbitrary bending are also investigated. As width and height of the rectangles increase, the intensity of bending beams increases. In addition, the field intensity distribution on bending beams can be tuned by varying the distance between the rectangles and the metal film. All of these findings can provide guidance in the design and optimization of bending beam generator, opening new possibilities in biosensing, optical trapping, micromanipulation, and optical integration.

Acknowledgments

The work is financially supported by National Natural Science Foundation of China (NSFC) (Grant No. 61575117), the Fundamental Research Funds for the Central Universities of Ministry of Education of China (Grant Nos. GK201601008, GK201603015, and GK201604003).

Appendix A. Supplementary material

Supplementary data associated with this article can be found in the online version at http://dx.doi.org/10.1016/j.optcom.2016.09.045.

References

[1] J. Baumgartl, M. Mazilu, K. Dholakia, Optically mediated particle clearing using Airy wave packets, Nat. Photonics 2 (11) (2008) 675–678.
[2] J. Arlt, V. Garces-Chavez, W. Sibbett, et al., Optical micromanipulation using a Bessel light beam, Opt. Commun. 197 (4) (2001) 239–245.
[3] M.V.B.N.L. Balazs, Nonspreading wave packets, Am. J. Phys. 4 (1979) 264–267.
[4] G.A. Siviloglou, J. Broky, A. Dogariu, et al., Observation of accelerating Airy beams, Phys. Rev. Lett. 99 (21) (2007) 213901.
[5] G.A. Siviloglou, D.N. Christodoulides, Accelerating finite energy Airy beams, Opt. Lett. 32 (8) (2007) 979–981.
[6] L. Carretero, P. Acebal, S. Blaya, et al., Nonparaxial diffraction analysis of Airy beams, Opt. Express 17 (25) (2009) 22432–22441.
[7] J. Broky, G.A. Siviloglou, A. Dogariu, et al., Self-healing properties of optical Airy beams, Opt. Express 16 (17) (2008) 12880–12891.
[8] I. Kaminer, R. Bekenstein, J. Nemirovsky, et al., Nondiffracting accelerating wave packets of Maxwell's equations, Phys. Rev. Lett. 108 (16) (2012) 163901.

[9] I.D. Chremmos, Z. Chen, D.N. Christodoulides, et al., Bessel-like optical beams with arbitrary trajectories, Opt. Lett. 37 (23) (2012) 5003–5005.
[10] P. Zhang, Y. Hu, T. Li, et al., Nonparaxial Mathieu and Weber accelerating beams, Phys. Rev. Lett. 109 (19) (2012) 193901.
[11] P. Aleahmad, M.A. Miri, M.S. Mills, et al., Fully vectorial accelerating diffraction-free Helmholtz beams, Phys. Rev. Lett. 109 (20) (2012) 203902.
[12] C. Alpmann, R. Bowman, M. Woerdemann, et al., Mathieu beams as versatile light moulds for 3D micro particle assemblies, Opt. Express 18 (25) (2010) 26084–26091.
[13] J. Zhao, P. Zhang, D. Deng, et al., Observation of self-accelerating Bessel-like optical beams along arbitrary trajectories, Opt. Lett. 38 (4) (2013) 498–500.
[14] E. Greenfield, M. Segev, W. Walasik, et al., Accelerating light beams along arbitrary convex trajectories, Phys. Rev. Lett. 106 (21) (2011) 213902.
[15] L. Froehly, F. Courvoisier, A. Mathis, et al., Arbitrary accelerating micron-scale caustic beams in two and three dimensions, Opt. Express 19 (17) (2011) 16455–16465.
[16] Y. Kaganovsky, E. Heyman, Wave analysis of Airy beams, Opt. Express 18 (8) (2010) 8440–8452.
[17] C. Genet, T.W. Ebbesen, Light in tiny holes, Nature 445 (7123) (2007) 39–46.
[18] W.L. Barnes, A. Dereux, T.W. Ebbesen, Surface plasmon subwavelength optics, Nature 424 (6950) (2003) 824–830.
[19] J. Lin, J. Dellinger, P. Genevet, et al., Cosine-Gauss plasmon beam: a localized long-range nondiffracting surface wave, Phys. Rev. Lett. 109 (9) (2012) 093904.
[20] A. Minovich, A.E. Klein, N. Janunts, et al., Generation and near-field imaging of Airy surface plasmons, Phys. Rev. Lett. 107 (11) (2011) 116802.
[21] A. Salandrino, D.N. Christodoulides, Airy plasmon: a nondiffracting surface wave, Opt. Lett. 35 (12) (2010) 2082–2084.
[22] A.E. Klein, A. Minovich, M. Steinert, et al., Controlling plasmonic hot spots by interfering Airy beams, Opt. Lett. 37 (16) (2012) 3402–3404.
[23] W. Liu, D.N. Neshev, I.V. Shadrivov, et al., Plasmonic Airy beam manipulation in linear optical potentials, Opt. Lett. 36 (7) (2011) 1164–1166.
[24] L. Li, T. Li, S.M. Wang, et al., Plasmonic Airy beam generated by in-plane diffraction, Phys. Rev. Lett. 107 (12) (2011) 126804.
[25] L. Li, T. Li, S.M. Wang, et al., Collimated plasmon beam: nondiffracting versus linearly focused, Phys. Rev. Lett. 110 (4) (2013) 046807.
[26] L. Li, T. Li, S.M. Wang, et al., Steering plasmon beam from a point source, Opt. Lett. 37 (24) (2012) 5091–5093.
[27] I. Epstein, A. Arie, Arbitrary bending plasmonic light waves, Phys. Rev. Lett. 112 (2) (2014) 023903.
[28] I. Epstein, A. Arie, Dynamic generation of plasmonic bottle-beams with controlled shape, Opt. Lett. 39 (11) (2014) 3165–3168.
[29] A. Libster-Hershko, I. Epstein, A. Arie, Rapidly accelerating Mathieu and Weber surface plasmon beams, Phys. Rev. Lett. 113 (12) (2014) 123902.
[30] H. Ko, H.C. Kim, M. Cheng, Light focusing at metallic annular slit structure coated with dielectric layers, Appl. Opt. 49 (6) (2010) 950–954.
[31] L. Verslegers, P.B. Catrysse, Z. Yu, et al., Planar lenses based on nanoscale slit arrays in a metallic film, Nano Lett. 9 (1) (2008) 235–238.
[32] X. Zhang, L. Yan, Y. Guo, et al., Enhanced far-field focusing by plasmonic lens under radially polarized beam illumination, Plasmonics 11 (1) (2016) 109–115.
[33] I. Dolev, I. Epstein, A. Arie, Surface-plasmon holographic beam shaping, Phys. Rev. Lett. 109 (20) (2012) 203903.
[34] X.M. Tang, L. Li, T. Li, et al., Converting surface plasmon to spatial Airy beam by graded grating on metal surface, Opt. Lett. 38 (10) (2013) 1733–1735.
[35] C. Guan, M. Ding, J. Shi, et al., Experimental observation and analysis of all-fiber plasmonic double Airy beams, Opt. Express 22 (15) (2014) 18365–18371.
[36] C. Guan, M. Ding, J. Shi, et al., Compact all-fiber plasmonic Airy-like beam generator, Opt. Lett. 39 (5) (2014) 1113–1116.
[37] Y. Lee, K. Hoshino, A. Alu, et al., Efficient directional beaming from small apertures using surface-plasmon diffraction gratings, Appl. Phys. Lett. 101 (4) (2012) 041102.
[38] Y. Liu, T. Zentgraf, G. Bartal, et al., Transformational plasmon optics, Nano Lett. 10 (6) (2010) 1991–1997.
[39] I. Epstein, Y. Lilach, A. Arie, Shaping plasmonic light beams with near-field plasmonic holograms, J. Opt. Soc. Am. B 31 (7) (2014) 1642–1647.
[40] L. Verslegers, P.B. Catrysse, Z. Yu, et al., Planar lenses based on nanoscale slit arrays in a metallic film, Nano Lett. 9 (1) (2008) 235–238.
[41] M.A. Ordal, L.L. Long, R.J. Bell, et al., Optical properties of the metals Al, Co, Cu, Au, Fe, Pb, Ni, Pd, Pt, Ag, Ti, and W in the infrared and far infrared, Appl. Opt. 22 (7) (1983) 1099–1119.
[42] D.E. Aspnes, J.B. Theeten, Spectroscopic analysis of the interface between Si and its thermally grown oxide, J. Electrochem. Soc. 127 (1980) 1359–1365.